https://dx.doi.org/10.1016/j.istruc.2022.08.097

Stainless steel ring strengthened removable dowel bar connection system: Effect of key parameters and design recommendations

Jiachen GUO[1] and Tak-Ming CHAN[1,*]

Department of Civil and Environmental Engineering, The Hong Kong Polytechnic University, Hong Kong, China

* Corresponding author: tak-ming.chan@polyu.edu.hk

Abstract

This paper numerically studies key parameters which affect the structural performance of the stainless steel ring strengthened removable dowel bar connection system. Finite element models were firstly validated against experimental test results in terms of the failure mode and load-deflection relationship. Then validated models were used to carry out the parametric investigation. The dowel bar diameter, the stainless steel ring length as well as the stainless steel ring thickness were studied with 90 generated models. According to the finite element analysis results, it was found that the vertical stiffness and ultimate load were enhanced with the increase of the dowel bar diameter. And the application of the stainless steel ring significantly relieved the compressive stress concentration at joint surface due to the expanded contact area. Close relationships were then observed between the ultimate load and the stainless steel ring thickness and length, respectively. Empirical equations were also derived to predict the ultimate load under the ultimate limit state (ULS). Meanwhile, under 20 kN service limit state (SLS), a close relationship was also found between the maximum compressive stress of concrete and the external diameter of the stainless steel ring. Through this two-stage design, the stainless steel ring strengthened removable dowel bar connection system will be more durable and reliable.

Keywords

Removable dowel bar connection system, dowel bar diameter, stainless steel ring length, stainless steel ring thickness, design recommendations.

1. Introduction

In jointed plain concrete pavement (JPCP) systems, the joint design has a significant impact on the structural performance of the whole system [1-4]. Generally, there are three main types of pavement joints including the contraction joint to relieve concrete tensile stress, expansion joint to create space for concrete expansion as well as construction joint to facilitate the pavement construction [1]. Among these joints, the contraction joint is the most important as the concrete is an anisotropic material which is strong in compression while weak in tension. Tensile cracks are easy to occur and propagate if the shrinkage of concrete is restricted. Therefore, pavement joints should be designed with the pavement slab free to expand and shrink without inducing any internal stress [5].

The traditional epoxy-coated dowel bar, as a commonly used pavement connection, is often designed with the diameter from 25 mm (1 in.) to 38 mm (1.5 in.) under different wheel loads [1, 2, 6, 7]. The main role of the dowel bar is to transfer the wheel load from one pavement slab to the adjacent panel through the bearing stress between dowel bar and concrete [8-10]. However, there are also critical issues in the dowel bar application including the severe stress concentration and steel corrosion.

Fig. 1(a) introduces the loading transfer mechanism of JPCP systems which is achieved by the relative deflection between adjacent pavement slabs. During the load transfer, as shown in Fig. 1(b), high bearing stresses are concentrated on the top and bottom of the dowel slot and concentrated tensile stresses were located at both sides. The severe compressive stress concentration will lead to the localised concrete crushing which

then deteriorates the joint effectiveness and reduce the loading transfer efficiency [11-14]. Regarding the tensile stress concentration, although Friberg et al. [15] firstly observed horizontal tensile cracks at dowel bar sides in 1930s. This type of joint distress was not comprehensively analysed until the development of the three-dimensional finite element analysis (FEA). Through the detailed contact modelling between the dowel bar and concrete, the tensile stress distribution around pavement connection was able to be visualised [9, 16-19]. To relieve the compressive stress concentration induced joint distresses, the shape of dowel bar was updated. Hu et al. [20] studied elliptical and rectangular dowel bars with large contact surfaces and test results showed that the bearing stress at the joint surface was effectively reduced under cyclic loads.

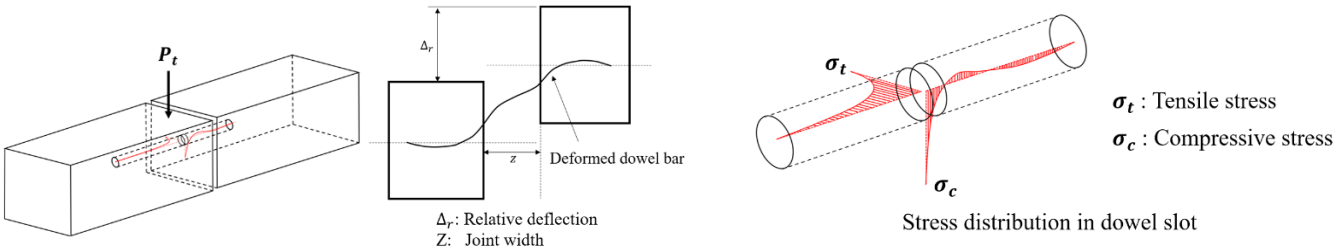

(a) (b)

Fig. 1. The load transfer in jointed plain concrete pavement system (a) load transfer mechanism, (b) stress distribution within the dowel slot.

To improve the corrosion resistance, a thin epoxy coating is attached on the surface of the steel dowel bar before installation. However, under fatigue loads, this thin coating is easy to be abraded, which results in the localised steel corrosion after water penetration and chloride ion exchange [21, 22]. Because of corrosion, the volume of the dowel bar is expanded and the effective section is reduced. As a result, the serious concrete crushing and oblonging, namely a void space around the dowel bar in concrete, will occur at pavement joint surface. The flow chart in Fig. 2 concludes the stress concentration and corrosion induced joint distresses. To avoid the corrosion related issues, non-corrosion materials like stainless steel and fibre reinforced polymer (FRP) were used by other researchers to replace the traditional structural steel [11, 14, 23-26].

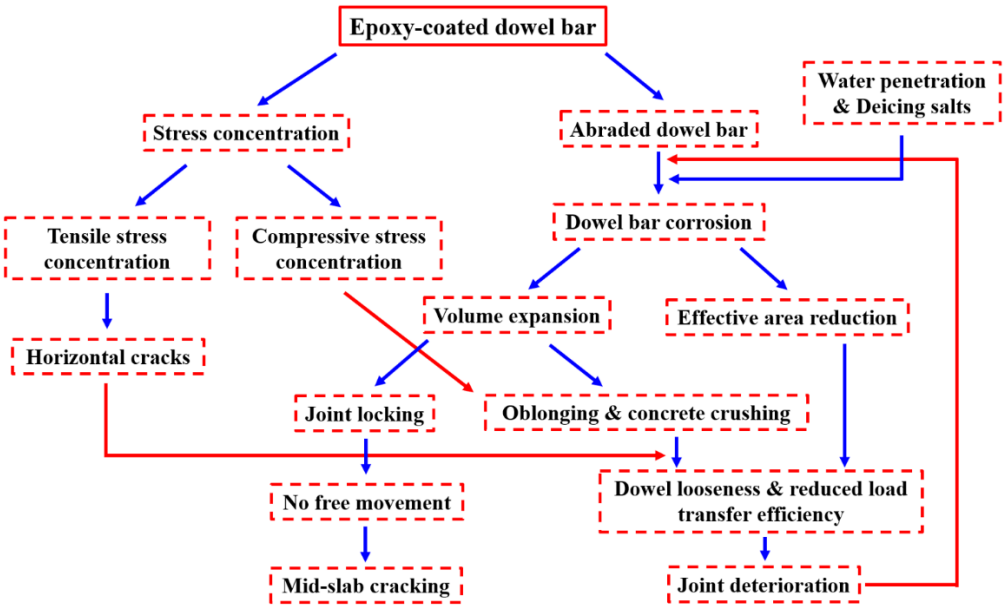

Fig. 2. The stress concentration and steel corrosion induced joint distress.

Over the last few decades, FEA had been adopted to model the jointed plain concrete pavement (JPCP) systems. Generally, developed finite element models could be divided into two types, including two-dimensional (2D) models and three-dimensional (3D) models. Regarding two-dimensional models, to simplify modelling process, a specific loading transfer efficiency was firstly incorporated to consider the role of dowel bar between pavement slabs [27-29]. To simulate the dowel-concrete interaction, vertical spring elements and contact elements were then employed to simulate the dowel bar load transfer [30-36]. Although these spring elements were also preferred in three-dimensional finite element models [37-44], this contact simulation was challenged by most of researchers and then replaced by the surface-to-surface contact modelling technique [9, 10, 16, 17, 19, 45-55].

To alleviate the stress concentration and corrosion related issues and achieve demountability, the stainless steel ring strengthened removable dowel bar connection was proposed and tested under monotonic load [56]. The objective of this paper is to further analyse the removable dowel bar connection system through FEA. The extended parametric analysis is conducted with the validated models to analyse the effects of key parameters

71 on the structural performance of the removable dowel bar connection system. Empirical equations to predict
72 the ultimate load and the maximum compressive stress under service load are also derived based on FEA
73 results.

74 **2. Finite element analysis**

75 Since only a limited number of specimens were tested experimentally, key parameters that influence the
76 structural performance of the removable dowel bar connection system were further investigated through FEA.
77 ABAQUS [57], a general-purpose software package, was used to develop the model of the removable dowel
78 bar connection system. Then the extensive parametric analysis was conducted to assess the effects of key
79 parameters.

80 **2.1 Finite element model**

81 As the removable dowel bar connection system consisted of several parts, in FEA, each part was developed
82 separately and then assembled together. Fig. 3(a) shows the constitution of the concrete block with the
83 removable dowel bar connection. The stainless steel ring and tube were cast into concrete during the pavement
84 slab fabrication while the stainless steel dowel bar was removable and inserted into stainless steel tube on site.
85 With the application of the L-shape steel plate, as shown in Fig. 3(b), the individual pavement block can be
86 lifted to achieve demountability after moving the dowel bar into one pavement block. Components of the
87 stainless steel ring strengthened removable dowel bar connection system were modelled by three-dimensional
88 eight-node solid elements with reduced integration (C3D8R) available in ABAQUS [57]. Fig. 4 shows
89 components of the removable dowel bar connection in FEA including the stainless steel dowel bar, the stainless
90 steel tube with slot as well as the stainless steel ring. The developed finite element model followed the
91 monotonic loading test arrangement which is shown in Fig. 5 [56]. The concrete block with the proposed

connection system was supported by a roller support at bottom and the other side of the dowel bar was supported by the fixing device. A thick steel plate and high-strength bolts were placed on the top to tighten the fixing device to the rigid block and avoid the unnecessary upward deformation. Regarding load arrangement, a rectangular steel block with 50 mm width was put on the top of concrete block at the joint to exert the vertical load and reduce the flexural deformation in concrete. The whole model displayed in Fig. 6 consists of the concrete block with the top loading block, removable dowel bar connection and fixing device. Based on experimental test results, most of specimens failed because of the severe concrete crushing at the joint surface and brittle shear cracks initiated near the loading block [56]. Therefore, as noted in Fig. 6(d), refined meshes were assigned in the concrete block at joint surface and near the loading block to capture typical failure modes.

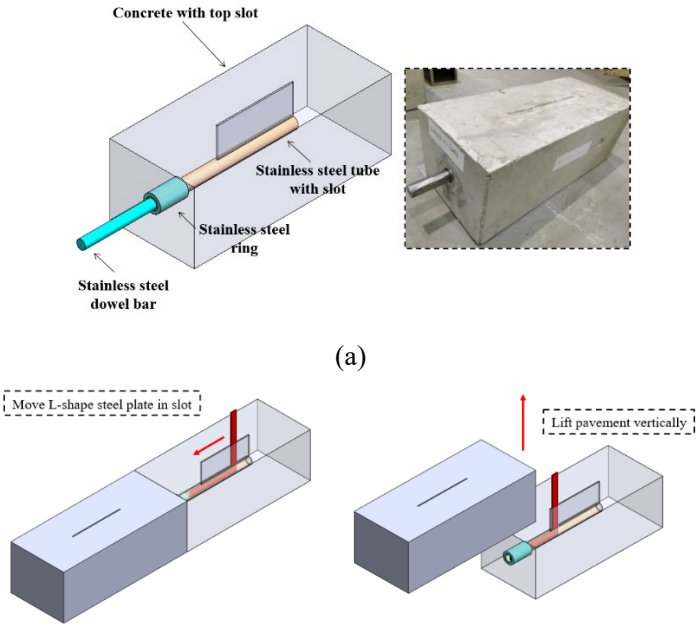

Fig. 3. Details of the removable dowel bar connection system (a) removable dowel bar connection system, (b) pavement replacement procedure.

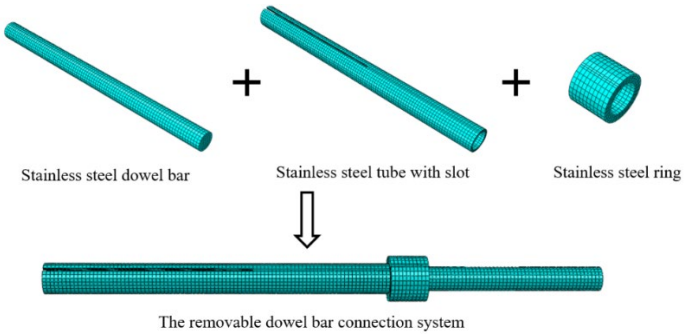

Fig. 4. Components of the removable dowel bar connection system.

103

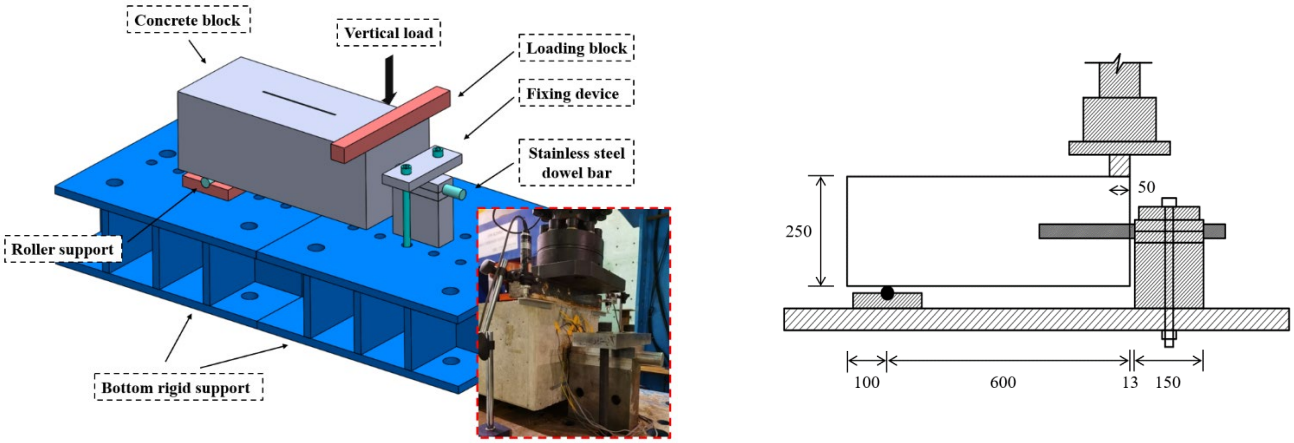

(a) (b)

Fig. 5. Experimental test setup (a) axonometric view, (b) schematic view (Unit: mm).

104

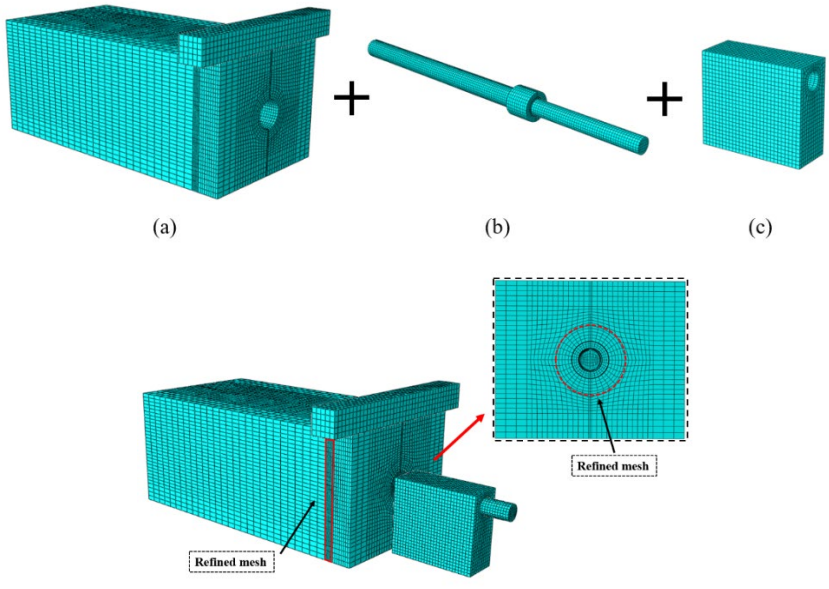

(d)

Fig. 6. Finite element model (a) concrete block with the loading block, (b) removable dowel bar connection, (c) fixing device, (d) assembled model.

105 In addition to the element type as well as the mesh size, another important aspect in FEA is the interaction

simulation between different components. In this model, the surface-to-surface contact modelling technique was adopted to simulate the actual contact behaviour and two different interaction properties were considered including IP1 and IP2. The interaction property IP1 was determined as “hard contact” along the normal direction and allowed separation after contact. The tangential behaviour was modelled by “penalty” type friction with a specific frictional coefficient. The interaction property IP1 was adopted to simulate the tangential behaviour between steel contacts with the frictional coefficient equal to 0.15. To model the contact between concrete and steel, the interaction property IP2 was developed and the frictional coefficient was equal to 0.35 which was same as the that adopted by Al-Humeidawi and Mandal [58]. In the surface-to-surface contact modelling, both master surface and slave surface should be defined. The master surface was stiffer than the slave surface and the mesh size of that was coarser at the contact surface to avoid convergence issues [57]. Following this principle, contact surface assignments in FEA are shown in Fig. 7 including the dowel to tube, dowel to fixing device, tube to concrete, tube to ring, ring to concrete and the loading block to concrete.

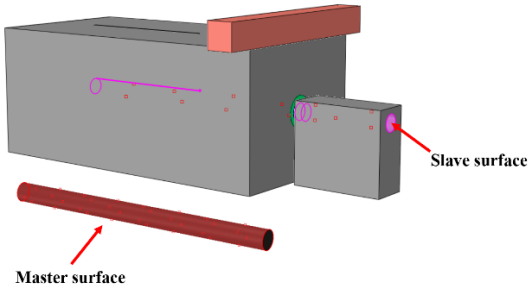

(a)

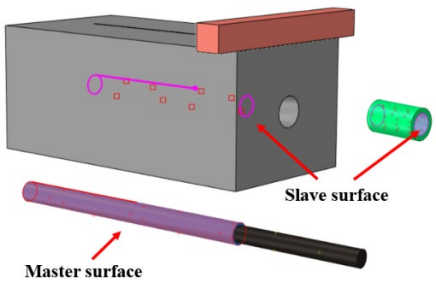

(b)

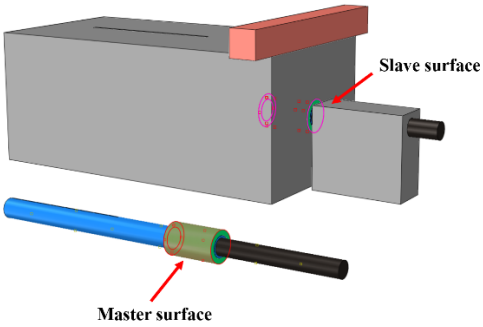

(c)

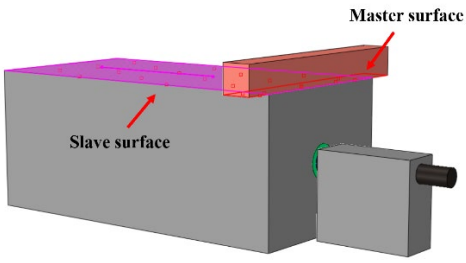

(d)

Fig. 7. Contact surface assignments in finite element model (a) dowel to tube and dowel to fixing device, (b) tube to ring and tube to concrete, (c) ring to concrete, (d) loading block to concrete block.

Boundary conditions of the finite element model also followed the experimental test settings [56]. As the contact between concrete and the roller support led to some convergence problems in FEA, to simplify the finite element model, the roller support under concrete block was replaced by a coupling constraint with the reference point RP-1 placed at bottom as Fig. 8(a) shows. The distance between RP-1 and joint surface is 600 mm which is the same as that in experimental tests [56]. The concrete block beyond the roller support was removed as it had no effect on the performance of the whole model. Displacements along the *Y* axis U2, along *Z* axis U3, rotation about *X* axis UR1 and along *Z* axis UR3 were restricted to simulate the roller support. In terms of the fixing device, the top steel plate and high-strength bolts were simplified to the fixed condition at the bottom which is displaced in Fig. 8(b). The displacement-type vertical load was exerted to the loading block through the reference point RP-2 and the coupling constraint as shown in Fig. 9.

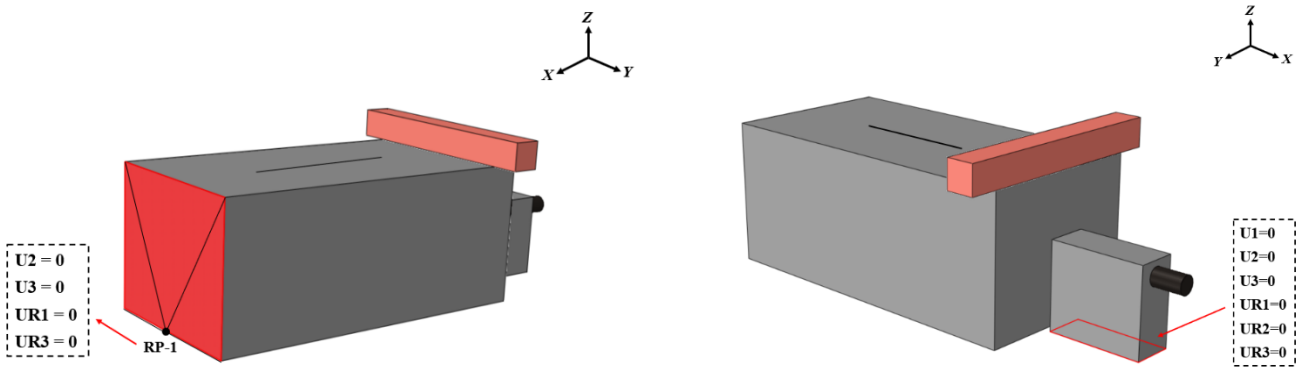

(a) (b)

Fig. 8. Boundary conditions of the finite element model (a) coupling constraint modelled roller support, (b) fixing device simulation.

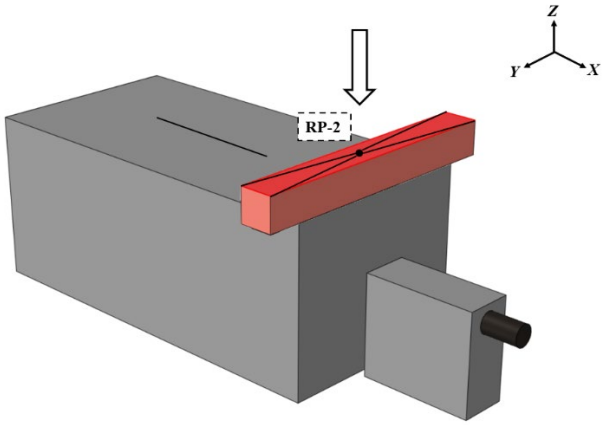

Fig. 9. Load arrangement in finite element analysis (FEA).

2.2 Material properties

2.2.1 Concrete material model

In FEA, the Concrete Damaged Plasticity (CDP) model, proposed by Lubliner et al. [59] and then modified by Lee and Fenves [60], was adopted to model the non-linear behaviour of concrete. The Concrete Damaged Plasticity model available in ABAQUS not only considers the unrecoverable plastic deformation stressed in plasticity model, but also involves the reduced elastic stiffness emphasised in damaged model [61, 62]. In the CDP model, the concrete uniaxial compressive stress-strain relationship was defined according to CEB Model Code 2010 [63] which is expressed in Eqs. (1) to (3), where σ_c is the concrete compressive stress; f_c is the concrete compressive strength; ε_c is the concrete compressive strain; ε_{cl} is the compressive strain at the compressive strength; $\varepsilon_{c,lim}$ is the limited compressive strain corresponding to $0.5f_c$ within the post peak stage; E_{ci} is the tangential modulus of elasticity of concrete at the origin; E_{cl} is the scant modulus of elasticity at the peak stress; k is the plasticity number. The descending branch beyond the limited compressive strain was determined by Eqs. (4) and (5) from CEB Model Code 1990 [64]. Relevant material parameters listed in Table 1 were obtained from the uniaxial compressive strength test and CEB Model Code 2010 [63]. And the uniaxial compressive stress-strain curve of concrete is shown in Fig. 10 with the elastic stage from zero to $0.4f_c$. The scant modulus of elasticity at the end of the elastic stage E_c was equal to 29.7 GPa as shown in Table 1. Other

parameters in CDP model such as the dilation angle ψ, equibiaxial compressive stress to uniaxial compressive stress σ_{b0}/f_{c0}, tensile meridian to compressive meridian K, eccentricity ϵ and viscosity parameter were equal to 38˚, 1.16, 0.667, 0.1 as well as zero, respectively [65].

$$\frac{\sigma_c}{f_c} = \left[\frac{k\eta - \eta^2}{1 + (k-2)\eta}\right] \tag{1}$$

$$\eta = \left(\frac{\varepsilon_c}{\varepsilon_{cl}}\right) \tag{2}$$

$$k = \left(\frac{E_{ci}}{E_{cl}}\right) \tag{3}$$

$$\sigma_c = \left[\left(\frac{1}{\frac{\varepsilon_{c,lim}}{\varepsilon_{cl}}}\xi - \frac{2}{(\frac{\varepsilon_{c,lim}}{\varepsilon_{cl}})^2}\right)\left(\frac{\varepsilon_c}{\varepsilon_{cl}}\right)^2 + \left(\frac{4}{\frac{\varepsilon_{c,lim}}{\varepsilon_{cl}}} - \xi\right)\left(\frac{\varepsilon_c}{\varepsilon_{cl}}\right)\right]^{-1} f_c \tag{4}$$

$$\xi = \frac{4\left[(\frac{\varepsilon_{c,lim}}{\varepsilon_{cl}})^2\left(\frac{E_{ci}}{E_{cl}} - 2\right) + 2\frac{\varepsilon_{c,lim}}{\varepsilon_{cl}} - \frac{E_{ci}}{E_{cl}}\right]}{\left[\frac{\varepsilon_{c,lim}}{\varepsilon_{cl}}\left(\frac{E_{ci}}{E_{cl}} - 2\right) + 1\right]^2} \tag{5}$$

The uniaxial tensile behaviour of concrete was modelled through the tensile stress versus crack width relationship in the CDP model. Before reaching the uniaxial tensile strength, the linear tensile stress-strain relationship was defined. Then for the post peak stage, Fig. 11 displays the mesh-independent tensile stress-crack width curve expressed as Eqs. (6) to (10) [63]. The uniaxial tensile strength f_t, fracture energy of concrete G_F, transition crack width w_t, crack opening width w_c are summarised in Table 2.

$$\sigma_t = f_t\left(1.0 - 0.8\frac{w}{w_1}\right) \; for \; w \le w_t \tag{6}$$

$$\sigma_t = f_t\left(0.25 - 0.05\frac{w}{w_1}\right) \; for \; w_t < w \le w_c \tag{7}$$

$$G_F = 0.73 f_c^{0.18} \tag{8}$$

$$w_t = \frac{G_F}{f_t} \tag{9}$$

$$w_c = \frac{5G_F}{f_t} \tag{10}$$

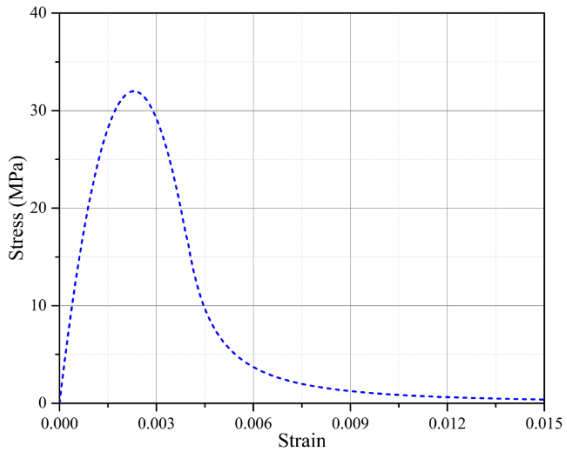

Fig. 10. Uniaxial compressive stress strain curve of concrete

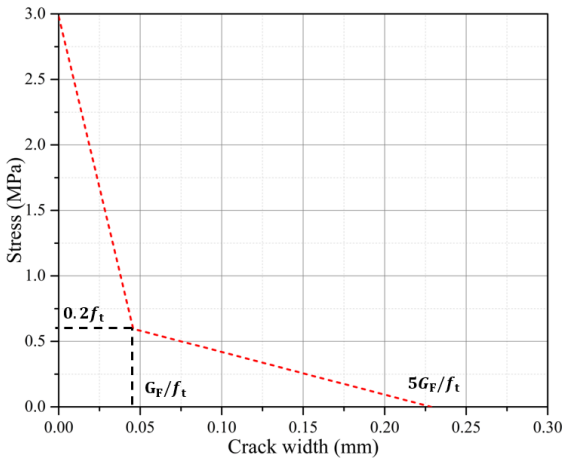

Fig. 11. Tensile stress-crack width relationship of concrete in finite element model

Table 1 Concrete material parameters (uniaxial compression).

f_c (MPa)	ε_{cl}	E_{ci} (GPa)	E_{cl} (GPa)	E_c (GPa)	k
31.92	0.0023	33.6	16.5	29.7	2.04

Table 2 Concrete material parameters (uniaxial tension).

f_t (MPa)	G_F (N/mm)	w_t (mm)	w_c (mm)
2.98	0.136	0.046	0.229

To consider the effects of concrete crushing and tensile microcracks on the reduced stiffness, damaged variables were incorporated in the CDP model to simulate the actual concrete behaviour. The reduced modulus of elasticity of concrete induced by the compressive damage could be found in Fig. 12(a) with the damaged modulus of elasticity equal to $E_c(1\text{-}d_c)$. ε_c^{pl} and ε_c^{in} in Fig. 12(a) are the plastic strain and inelastic strain, respectively. The compressive damage variable d_c was determined with the concrete compressive stress σ_c and plastic strain ε_c^{pl} following Eq. (11) [66]. Fig. 12(b) plots the concrete compressive damage variable d_c in FEA. The concrete tensile damage variable was defined proportionally to the energy dissipated by forming cracks, which was calculated by A_s/A_t as shown in Fig. 13(a), where, A_s is the shade area when tensile stress is equal to σ_t. A_t is the total area under the tensile stress-crack width curve which is equal to the fracture energy G_F. Therefore, the tensile damage variable d_t was calculated following Eqs. (12) and (13) as plotted in Fig. 13(b).

$$d_c = 1 - \frac{\sigma_c E_c^{-1}}{\varepsilon_c^{pl}\left(\frac{1}{b_c} - 1\right) + \sigma_c E_c^{-1}}, b_c = 0.7 \tag{11}$$

$$d_t = \frac{f_t\left(w - 0.4\frac{w^2}{w_t}\right)}{G_F}, w \le w_t \tag{12}$$

$$d_t = \frac{\left[f_t\left(0.125 - 0.025\frac{w}{w_t}\right)(w_c - w)\right]}{G_F}, w_t < w \le w_c \tag{13}$$

166

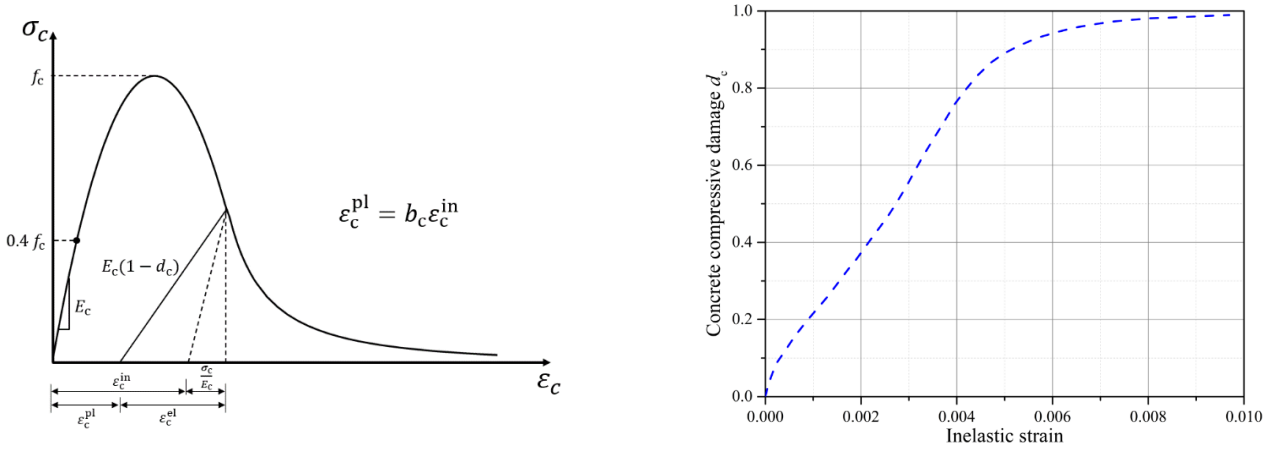

(a) (b)

Fig. 12. Concrete compressive damage (a) uniaxial concrete compressive behaviour with compressive damage, (b) compressive damage variable d_c in FEA.

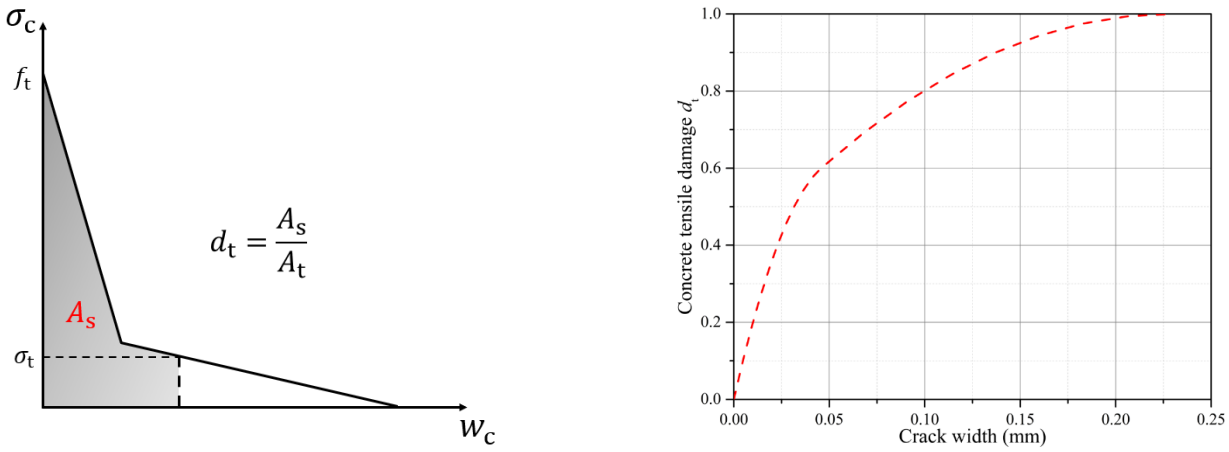

(a) (b)

Fig. 13. Concrete tensile damage (a) determination of the tensile damage variable d_t, (b) tensile damage variable in FEA.

167 2.2.2 Stainless steel material model

168 Stainless steel has been gradually used as the construction material in different structural applications due to

169 its higher corrosion resistance and excellent mechanical properties [67-69]. Significant strain hardening

behaviour could be observed in stainless steel material tests [70-72]. To accurately model the 304 authentic stainless steel material in FEA, as shown in Fig. 14, circular coupons milled from the stainless steel dowel bar and curved coupons extracted from the stainless steel tube were tested together with experimental tests. After obtaining the nominal stress-strain curves from coupon tests [56], the true stress-strain curves were then derived through Eqs. (14) and (15). Where σ_t and ε_t are true stress and true strain, respectively. The nominal and true stress-strain curves of the stainless steel dowel bar and tube are plotted in Fig. 15. Since the deformation of steel ring is relatively small, it was modelled as the elastic part to simplify the finite element model. The modulus of elasticity was determined from the material certificate provided from by the manufacturer. Relevant material parameters are summarised in Table 3.

$$\sigma_t = \sigma(1 + \varepsilon) \tag{14}$$

$$\varepsilon_t = \ln(1 + \varepsilon) \tag{15}$$

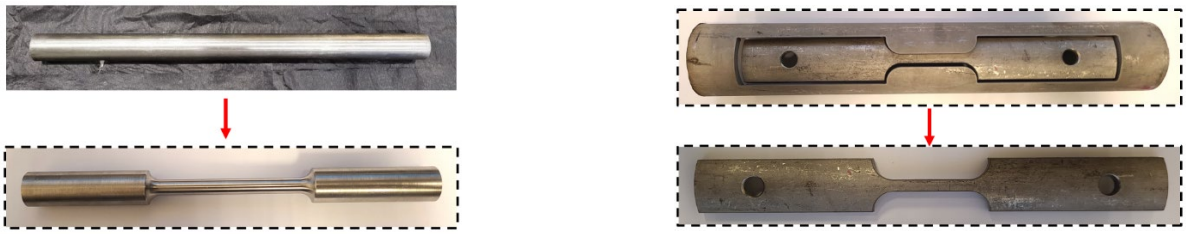

(a) (b)

Fig. 14. Stainless steel coupons (a) circular coupon milled from stainless steel dowel bar, (b) curved coupon cut from stainless steel tube.

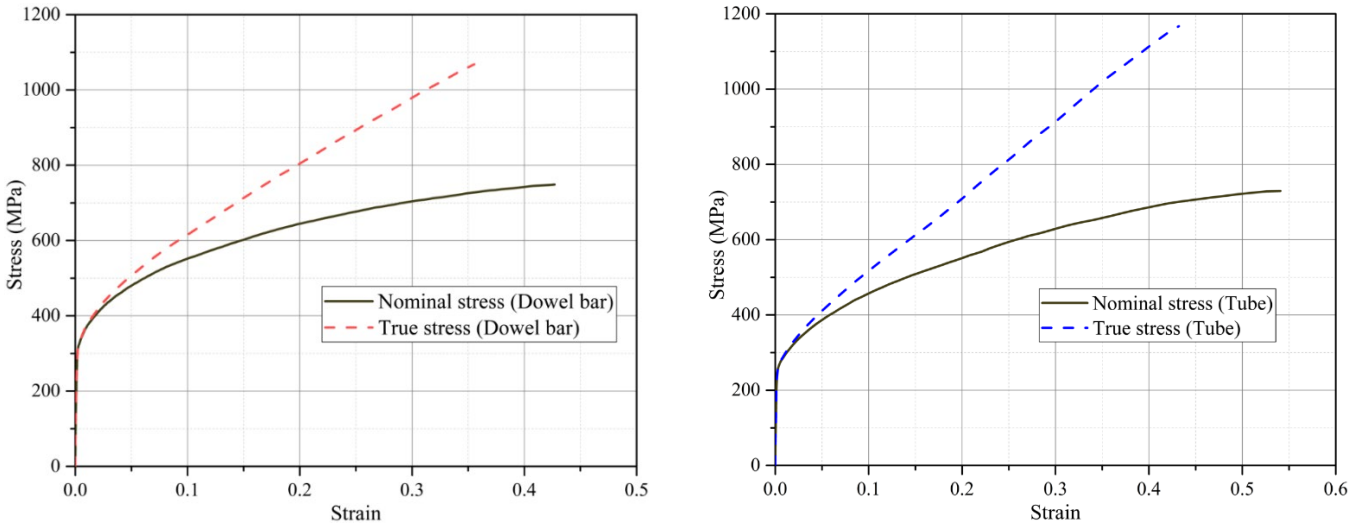

(a) (b)

Fig. 15. Stress-strain curves (a) stainless steel dowel bar, (b) stainless steel tube.

Table 3 Material properties of 304 authentic stainless steel.

Stainless steel	Modulus of elasticity E_s (GPa)	Yield strength $f_{y(0.2)}$ (MPa)	Ultimate strength f_u (MPa)	Elongation ε_f (%)
Ring	190.0	N.A.	N.A.	N.A.
Dowel bar	190.3	327.7	748.0	47
Tube	190.2	269.1	729.0	57

2.3 Model validation

The finite element models were validated with the experimental test results in terms of the failure mode as well as load-deflection relationship [56]. Fig. 16 shows the load deflection curves of specimens 32D and 32D4T as well as 32D4T10R100L from experimental tests and FEA, where 32D, 4T and 10R100L refer to the 32 mm dowel bar, 4 mm thickness stainless steel tube and 10 mm thickness stainless steel ring with 100 mm length, respectively. It was found that a close match was achieved in terms of load-deflection curves from experimental tests and FEA. Except for the load-deflection relationship, failure modes in FEA were also similar to those observed in experimental tests. For the localised concrete crushing, it initiated on the top of the dowel slot and then propagated with the increase of the vertical load. While brittle shear cracks occurred at the end of experimental tests once reaching the concrete shear strength. The concrete crushing failure in FEA was described by concrete compressive damage variables d_c shown in Fig. 17. Shear cracks in model

192 32D4T10R100L were simulated by concrete tensile damage variables d_t as displayed in Fig. 18. Table 4 lists
193 the ultimate load of each specimen from both the numerical simulation and experimental test. The low
194 Coefficient of Variation (CoV) indicates the accuracy of numerical simulation. The difference between the
195 predicted and test load was lower than 10 percent as shown in Fig. 19.

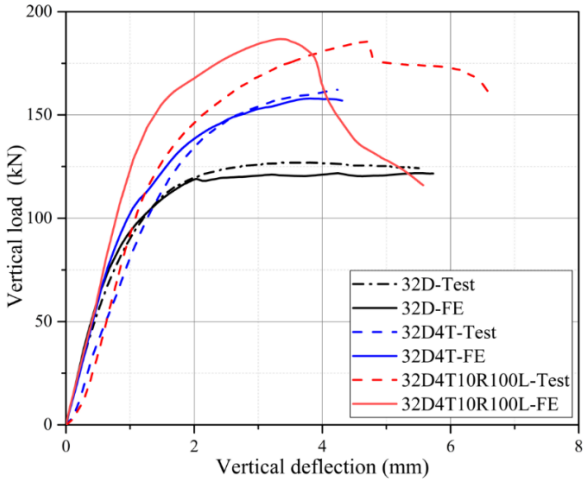

Fig. 16. Load-deflection curves of 32D, 32D4T and 32D4T10R100L.

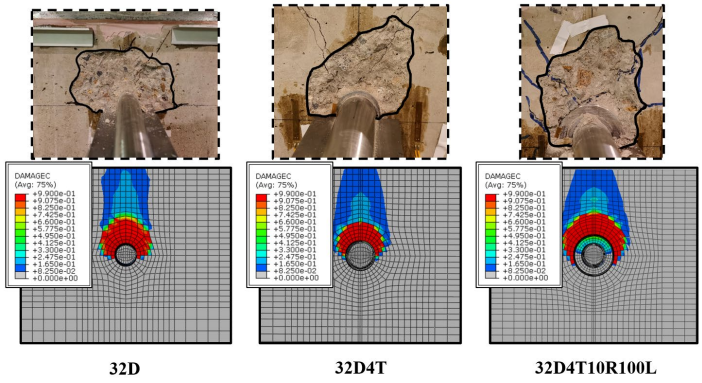

Fig. 17. Localised concrete crushing failure in tests and FEA.

196

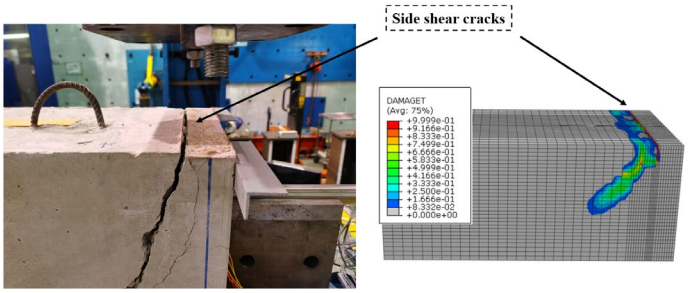

Fig. 18. Brittle shear cracks in 32D4T10R100L.

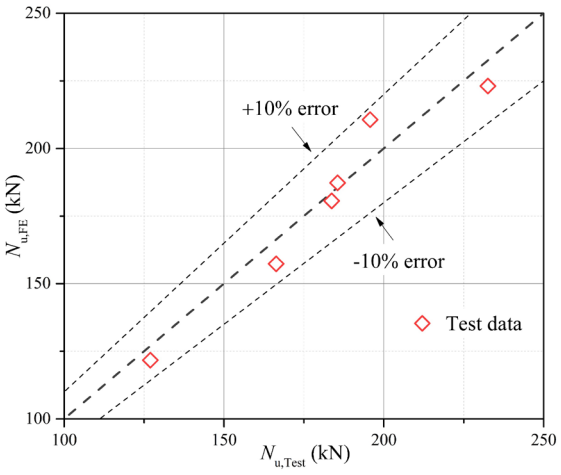

Fig. 19. Ultimate load of each specimen from the experimental test and FEA.

197 Table 4 Ultimate loads obtained from experimental tests and finite element analysis.

Specimen ID	Experimental test, $N_{u,Test}$ (kN)	Finite element analysis, $N_{u,FE}$ (kN)	$N_{u,Test}/N_{u,FE}$
32D	126.97	121.70	1.04
32D4T	166.29	157.36	1.06
32D4T10R50L	183.68	180.62	1.02

32D4T10R100L	185.55	187.28	0.99
32D4T20R50L	195.71	210.64	0.93
32D4T20R100L	232.59	223.10	1.04
		Mean	1.01
		CoV	0.043

3. Parametric investigation

To comprehensively analyse factors which have significant influences on the structural behaviour of the removable dowel bar connection system, the parametric study was conducted with the validated finite element model. In the design of jointed plain concrete pavement (JPCP) systems, the diameter of the epoxy coated steel dowel bar ranges from 25 mm (1 in.) to 38 mm (1.5 in.) [1, 2, 6, 7]. Therefore, 25 mm, 32 mm as well as 38 mm diameter dowel bars were incorporated in the parametric analysis. The stainless steel ring thickness as well as length were also studied to analyse the effect of the stainless steel ring on improving the ultimate load and relieving the compressive stress concentration. A total of 90 numerical models were developed and analysed.

3.1 Stainless steel ring thickness

Stainless steel ring can expand the contact area between connection and steel and therefore improve the ultimate load and relieve the compressive stress concentration. As can be seen in each column of Table 5, Table 6 and Table 7, the ultimate load of the specimen increased with the thickness of the stainless steel ring. Specifically, a relationship based on regression analysis was observed in Fig. 20 between the ultimate load and steel ring thickness. In experimental tests, nonlinear load-deflection relationships indicated the occurrence of the severe localised concrete crushing at joint surface. To evaluate the deflection response, the yield displacement Δ_y was defined at the intersection of the tangent of the load-deflection curve and the horizontal line passing the ultimate load. The corresponding vertical load at the yield deflection was regarded as the yield load N_y [73, 74]. The initial stiffness, namely the slope of the tangent of the load-deflection relationship, was

determined by the linear regression analysis. Table 8 summarises the yield load and initial stiffness of each model with the 32 mm diameter dowel bar and the stainless steel ring with different thicknesses. As found in Fig. 21, the initial stiffness and yield load increased with the thickness of the stainless steel ring.

Table 5 Ultimate loads of models with 25 mm diameter dowel bar (kN).

Thickness (mm) \ Length (mm)	25	50	75	100	125	150
5	121.5	132.8	141.1	146.7	151.4	156
10	133.9	144.5	154.6	161.5	167.4	173.4
15	150.5	160.7	170.1	178.1	186.2	194.3
20	165.5	178.6	187.5	195.7	204.1	215.5
25	180.1	195.3	205.2	213.3	227.6	240.2

Table 6 Ultimate loads of models with 32 mm diameter dowel bar (kN).

Thickness (mm) \ Length (mm)	25	50	75	100	125	150
5	166.3	168.2	170.6	172.8	176.7	179.6
10	174.5	180.6	182.2	187.3	192.8	197.6
15	185.3	194.5	197.1	204.1	211.1	217.0
20	196.2	210.6	214.8	223.1	231.4	237.6
25	210.5	226.5	232.8	243.2	252.2	258.5

Table 7 Ultimate loads of models with 38 mm diameter dowel bar (kN).

Thickness (mm) \ Length (mm)	25	50	75	100	125	150
5	184.2	189.8	194.9	198.4	202.7	206.9
10	197.1	202.4	207.7	214.3	219.4	223.4
15	205.6	213.5	218.8	225.5	234.4	243.7
20	213.0	225.9	235.7	244.2	254.6	265.0
25	227.4	241.8	254.9	265.7	279.0	291.2

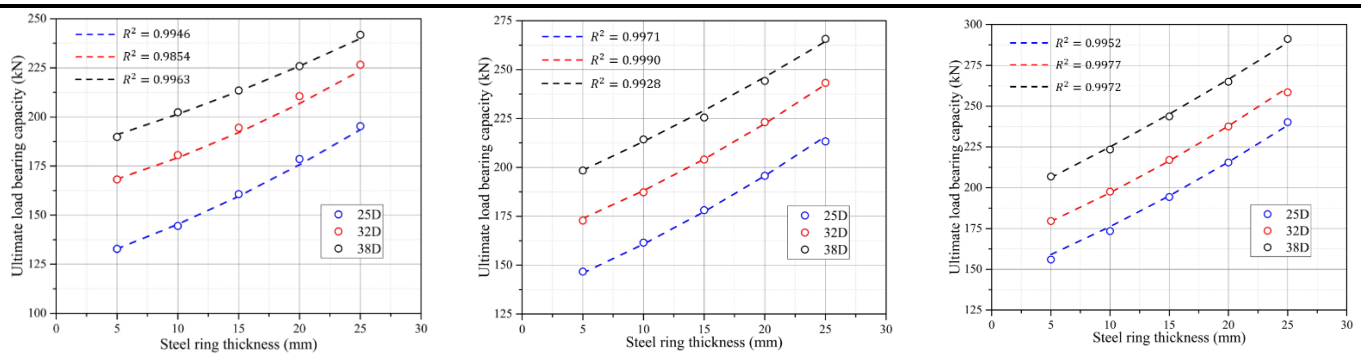

(a) (b) (c)

Fig. 20. Relationship between ultimate load bearing capacity and steel ring thickness (a) 50 mm-length stainless steel ring, (b) 100 mm-length stainless steel ring, (c) 150 mm-length stainless steel ring.

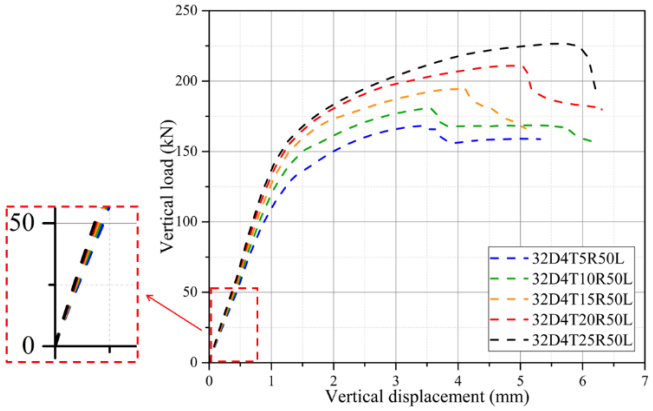

Fig. 21. Load-deflection relationship of specimens with a 32 mm dowel bar.

Table 8 Yield loads and initial stiffnesses of models with the stainless steel ring.

Specimen ID	Yield load N_y (kN)	Initial stiffness k (kN/mm)
32D4T5R50L	134.3	116.85
32D4T10R50L	149.4	121.33
32D4T15R50L	161.1	126.58
32D4T20R50L	168.2	132.28
32D4T25R50L	172.2	139.89

As reported by other researchers, the maximum shear force transferred by the individual dowel bar ranging from 5.85 kN to 20 kN with different subbase layers [2, 8, 14, 20, 22, 40, 46, 75]. Therefore, considering the most critical case, 20 kN was regarded as the service load to evaluate the compressive stress. The maximum normal contact stress in the concrete block, namely the peak compressive stress at joint surface, was obtained from FEA and shown in Fig. 22. The range separated by dash lines is the stainless steel ring thickness. It should be noted that contact stresses of specimen 25D, 32D as well as 38D exceed the concrete compressive strength, which may induce the concrete bearing failure under repeated loads. However, after the application of the stainless steel ring, the contact stress was reduced effectively and lower than the concrete compressive strength.

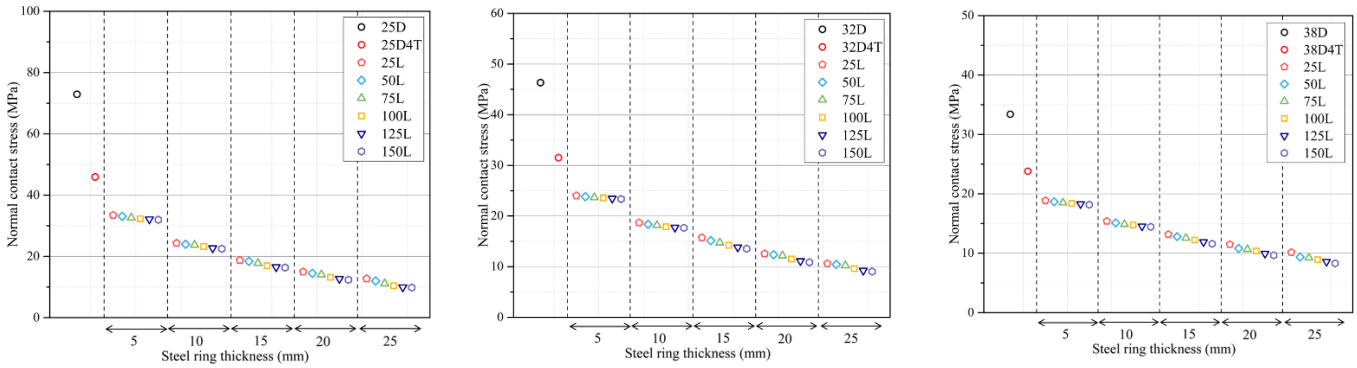

(a) (b) (c)

Fig. 22. Maximum normal contact stress predicted from FEA under 20 kN. (a) models with 25 mm diameter dowel bar, (b) models with 32 mm diameter dowel bar, (c) models with 38 mm diameter dowel bar.

3.2 Stainless steel ring length

Apart from the stainless steel ring thickness, the length of the ring part also influences the ultimate load and maximum compressive stress. With the long stainless steel ring, as shown in Fig. 23, the distribution of contact stress within the dowel slot became more uniform. Thus, the concentrated compressive stress in concrete at joint surface was reduced. Meanwhile, a close linear relationship was also observed between the ultimate load and steel ring length with a higher coefficient of determination (R^2) as can be seen from Fig. 24.

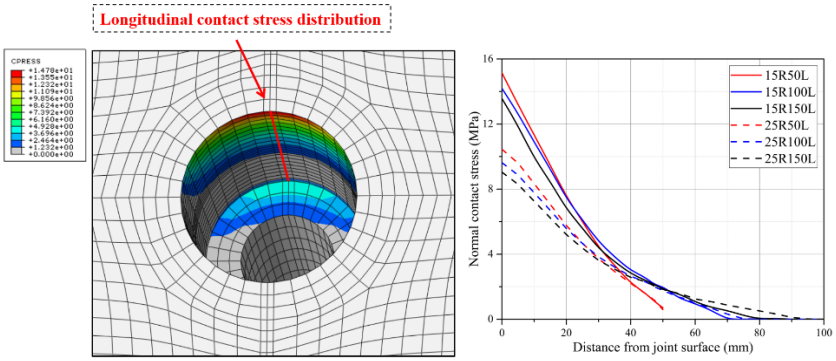

Fig. 23. Longitudinal distribution of the normal contact stress along dowel slot (32 mm dowel bar).

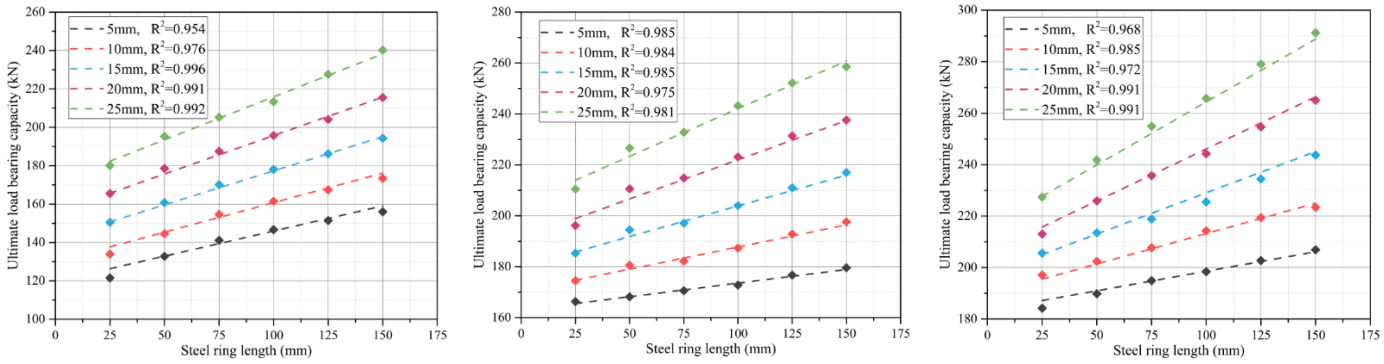

(a) (b) (c)

Fig. 24. Relationship between ultimate load bearing capacity and steel ring length (a) 25 mm dowel bar, (b) 32 mm dowel bar, (c) 38 mm dowel bar.

Furthermore, from Fig. 25, it is clearly found that the ultimate load displacement Δ_u increases with the stainless steel ring length. Table 9 summarises the initial stiffness k, yield load N_y and displacement Δ_y as well as ultimate load N_u and the corresponding displacement Δ_u of models with the 25 mm thickness stainless steel ring. Although comparable ultimate loads were achieved in specimens with different diameter dowel bars, ultimate displacements Δ_u and ratios Δ_u/Δ_y were totally different. The low initial stiffness and large Δ_u and Δ_u/Δ_y indicate the ultimate load is hard to be fully utilised unless with the large relative deflection between adjacent slabs. As a result, to improve the driving comfortability and achieve an effective load transfer, 25 mm diameter dowel bar is not suggested under heavy wheel loads.

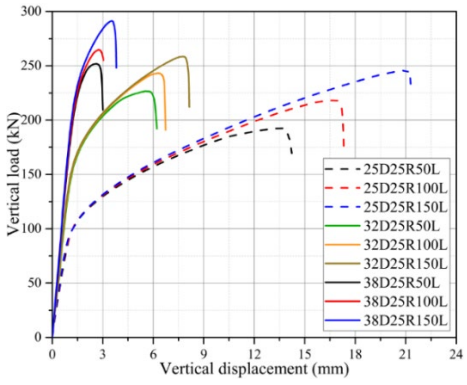

Fig. 25. Load-deflection relationship related to different dowel bar diameters and steel ring length.

Table 9 Deflection responses of specimens with the 25 mm thickness stainless steel ring.

Specimen ID		k (kN/mm)	N_y (kN)	Δ_y (mm)	N_u (kN)	Δ_u (mm)	Δ_u/Δ_y
25D25R	50L	100.31	115.1	1.92	192.4	13.55	7.06
	100L		120.3	2.18	218.3	16.75	7.68

	150L		123.9	2.45	245.6	20.99	8.57
	50L		171.2	1.60	226.6	5.54	3.46
32D25R	100L	141.27	177.0	1.72	243.2	6.30	3.66
	150L		181.3	1.83	258.5	7.76	4.24
	50L		220.9	1.48	251.8	2.56	1.73
38D25R	100L	169.66	229.9	1.56	264.7	2.79	1.79
	150L		243.7	1.72	291.2	3.54	2.06

3.3 Dowel bar diameter

The diameter of the dowel bar not only influences the ultimate load, but also has a huge impact on the joint stiffness. Using large diameter dowel bars can increase the contact area between the steel and concrete and therefore enhance the ultimate load. In addition, with the large flexural rigidity, models with the 38 mm diameter dowel bar have high initial stiffnesses as displayed in Figs. 25 and 26. Although applying the stainless steel ring can also improve the initial stiffness, this effect is not significant compared with increasing the dowel bar diameter. Increasing the stainless steel ring thickness five times (from 5 mm to 25 mm) can enhance the vertical stiffness by 19 percent while enlarging the dowel bar diameter by 50 percent (from 25 mm to 38) mm increases the stiffness by near 70 percent. Besides, the failure mode of the model is also changed with the dowel bar diameter. Compared with the model 25D and 32D, an obvious load drop was observed in model 38D which was caused by the initiation of the brittle shear cracks.

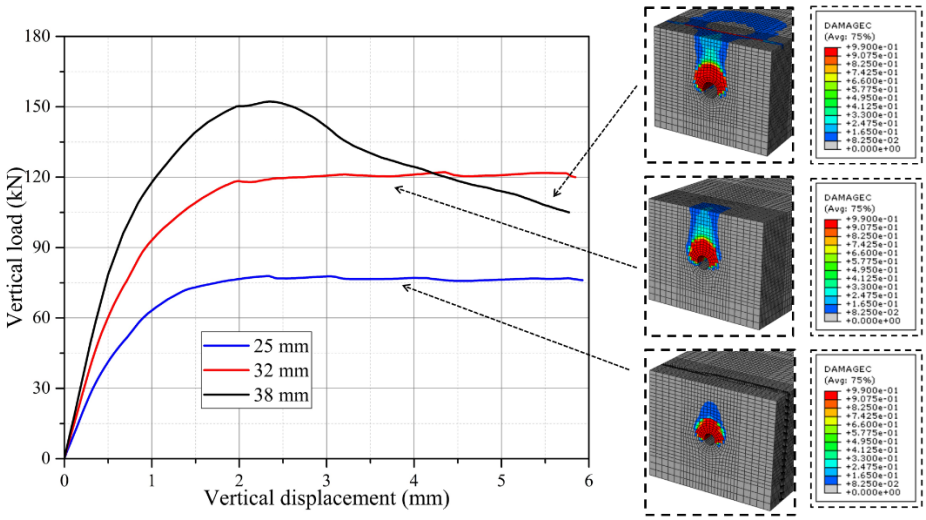

Fig. 26. Load-deflection relationship of specimens with different dowel bar diameters.

4. Evaluation of key parameters

Through the comprehensive FEA, key parameters affecting the structural behaviour of the stainless steel ring strengthened removable dowel bar connection are assessed and compared. For the dowel bar diameter, this factor has a significant impact on the improving the stiffness of the whole connection system. In terms of stainless steel ring, this part is applied to improve the ultimate load and relieve the compressive concentration. After applying the stainless steel ring, the contact area between concrete and steel is expanded and the induced contact stress is reduced. Additionally, increasing the length of the stainless steel ring also promotes the uniform distribution of contact stress within dowel slot and further reduces the normal contact stress at joint surface.

5. Design recommendations

From both experimental tests as well as the comprehensive FEA, the structural behaviour of the stainless steel ring strengthened removable dowel bar connection system has been thoroughly analysed. To instruct the design of the stainless steel ring strengthened removable dowel bar connection system, Eqs. (16) to (18) based on close relationships between the stainless steel ring length, thickness and the ultimate load were derived to predict ultimate loads of specimens with the stainless steel ring. The ultimate loads of specimens 25D4T, 32D4T as well as 38D4T were also incorporated as constants in design equations, respectively. Close predictions achieved by proposed equations are shown in dash lines of Fig. 24.

For specimens with 25 mm dowel bar,

$$N_u = (0.00926t + 0.2155)l + 0.0357t^2 + 1.498t + 111.4 \quad (16)$$

For specimens with 32 mm dowel bar,

$$N_u = (0.0134t + 0.043)l + 0.0394t^2 + 0.905t + 157.4 \quad (17)$$

For specimens with 38 mm dowel bar,

$$N_u = (0.0169t + 0.0673)l + 0.0241t^2 + 0.88t + 178.4 \quad (18)$$

where t and l are the thickness and length of the stainless steel ring, respectively.

In addition to the ultimate load, the structural performance of the stainless steel ring strengthened removable dowel bar connection under the service load also needs to be analysed. As plotted in Fig. 22, the normal contact stress at joint surface was reduced with the stainless steel ring thickness. Normal contact stresses of models with the stainless steel ring under 20 kN service load are summarised in Tables 10 to 12. To simplify the design, average contact stresses of models with the same thickness stainless steel ring were adopted. As a result, a power relationship was found between the normal contact stress and the diameter ratio d/d_0 as expressed by Eq. (19) and shown in Fig. 27, where $\sigma_{0,max}$ is the referenced normal contact stress of the model with the dowel bar; $\sigma_{s,max}$ is the normal contact stress of the model strengthened by stainless steel ring; d_0 and d are the dowel bar diameter and the external diameter of the stainless steel ring, respectively. After obtaining normal contact stresses of models 25D, 32D and 38D, it is possible to calculate the contact stresses of models with the stainless steel ring following the power relationship proposed in Eq. (19).

$$\sigma_{max} = \frac{\sigma_{0,max}}{(\frac{d}{d_0})^{1.5}} \quad (19)$$

Table 10 Normal contact stress of models with 25 mm diameter dowel bar (MPa).

Length (mm) \ Thickness (mm)	5	10	15	20	25
25	33.43	24.34	18.74	14.96	12.73
50	33.09	23.98	18.39	14.49	12.00
75	32.64	23.74	17.81	14.05	11.14
100	32.30	23.23	16.96	13.20	10.45
125	32.14	22.69	16.54	12.72	9.94
150	31.98	22.49	16.36	12.38	9.83
Average	32.60	23.40	17.47	13.63	11.02

Table 11 Normal contact stress of models with 32 mm diameter dowel bar (MPa).

Length (mm) \ Thickness (mm)	5	10	15	20	25
25	24.02	18.67	15.73	12.55	10.62
50	23.81	18.37	15.14	12.37	10.45
75	23.68	18.17	14.74	12.18	10.23
100	23.55	17.88	14.19	11.52	9.62
125	23.46	17.73	13.82	11.13	9.23
150	23.35	17.66	13.56	10.87	9.04
Average	23.65	18.08	14.53	11.77	9.87

Table 12 Normal contact stress of models with 38 mm diameter dowel bar (MPa).

Length (mm) \ Thickness (mm)	5	10	15	20	25
25	18.87	15.40	13.17	11.48	10.15
50	18.66	15.11	12.79	10.81	9.35
75	18.51	14.87	12.57	10.67	9.24
100	18.38	14.74	12.23	10.39	8.91
125	18.29	14.54	11.89	9.94	8.57
150	18.17	14.45	11.59	9.65	8.30
Average	18.48	14.86	12.37	10.49	9.09

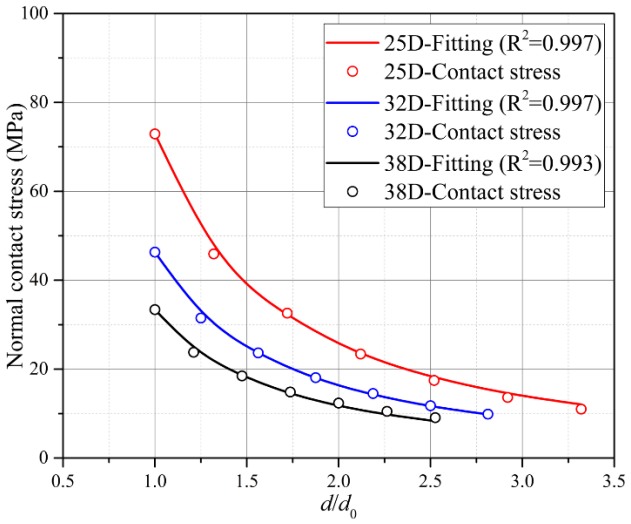

Fig. 27. Relationship between the normal contact stress and the diameter ratio.

To avoid the localised concrete bearing failure, the thickness of the stainless steel ring could be determined by Eqs. (19) after considering the allowable bearing stress. According to American Concrete Institute (ACI) subcommittee 325 [76], the allowable bearing stress is related to the dowel bar diameter and expressed as Eq.

(20). Where f_b is the allowable bearing stress, f_c is the concrete compressive strength, d is the dowel bar diameter. In the finite element model, the concrete compressive strength is 31.92 MPa. Therefore, the allowable bearing stress of models with the 25 mm, 32 mm as well as 38 mm diameter dowel bar are 31.92 MPa, 29.15 MPa and 26.64 MPa, respectively.

$$f_b = f_c(4 - d_0/25.4)/3 \quad (20)$$

However, the effects of concrete age as well as the number of loading cycles are not considered in Eq. (20). To comprehensively analyse all factors, the allowable bearing stress proposed in CEB-FIP Model Code 2010 were used [63]. Firstly, the fatigue compressive strength of concrete $f_{c,fat}$ was calculated by Eqs. (21) and (22) considering the concrete age and cement type, where, $\beta_{cc}(t)f_c$ is the concrete compressive strength at different age; s=0.2 when CEN 52.5 N cement is used; $\beta_{c,sus}(t, t_0)$ is taken as 0.85 under fatigue loads. According to the design codes, the new constructed rigid concrete pavement should be designed with 40 years' service life and to bear 10^6 to 10^8 cycles of wheel loads [2, 3, 77, 78]. Therefore, the corresponding fatigue concrete compressive strength is 30.30 MPa. To ensure no concrete bearing failure after millions of cyclic wheel loads, the allowable bearing stress was then determined by the typical S-N relationship of concrete under compression as expressed from Eqs. (23) to (27) and shown in Fig. 28. Where, N is the total number of loading cycles; $S_{c,max}$ is the maximum compressive stress ratio which is determined by the maximum compressive stress at joint surface under 20 kN and $S_{c,min}$ is equal to 0. Therefore, considering 10^6 to 10^8 loading cycles, the allowable bearing stress ranges from 13.64 MPa to 17.80 MPa. Then the corresponding stainless steel ring thickness is calculated following Eqs. (19).

$$f_{c,fat} = \beta_{cc}(t) f_c \beta_{c,sus}(t, t_0)\left(1 - \frac{f_c}{400}\right) \quad (21)$$

$$\beta_{cc}(t) = exp\left\{s\left[1 - \left(\frac{28}{t}\right)^{0.5}\right]\right\} \quad (22)$$

$$log\ N = \frac{8}{(Y-1)}\left(S_{c,max}-1\right)\ (logN \le 8) \tag{23}$$

$$log\ N = 8 + \frac{8\ln(10)}{(Y-1)}\left(Y - S_{c,min}\right) log\left(\frac{S_{c,max}-S_{c,min}}{Y-S_{c,min}}\right)(logN > 8) \tag{24}$$

$$Y = \frac{0.45 + 1.8S_{c,min}}{1 + 1.8S_{c,min} - 0.3S_{c,min}^2} \tag{25}$$

$$S_{c,max} = \left|\sigma_{c,max}\right|/f_{c,fat} \tag{26}$$

$$S_{c,min} = \left|\sigma_{c,min}\right|/f_{c,fat} \tag{27}$$

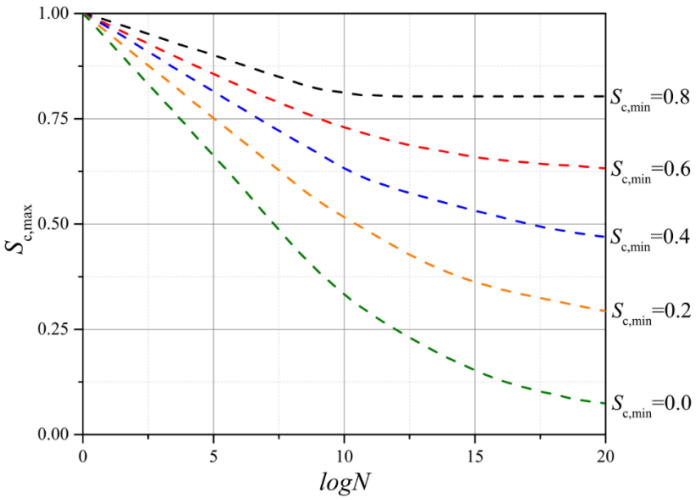

Fig. 28. Typical S-N relationship of concrete under compression.

6. Conclusion

In this paper, detailed FEA of the stainless steel ring strengthened removable dowel bar connection system has been conducted. Finite element models were validated against the experimental results in terms of failure modes and load-deflection relationships. After validation, a total 90 models were developed and parameters including the stainless steel ring thickness, length as well as the dowel bar diameter were comprehensively analysed. From the parametric analysis, some conclusions could be summarised as follows.

1. The large diameter dowel bar (38 mm) could improve the vertical stiffness and ultimate load of the connection system. While a different failure mode, namely brittle shear cracks, are observed in specimen with the 38 mm diameter dowel bar.

2. The stainless steel ring expands the contact area between steel and concrete and effectively relieves the compressive stress concentration. Therefore, the ultimate load is increased and the maximum compressive stress under service load is reduced.
3. Close relationships are found between the ultimate load and the stainless steel ring length and thickness, respectively.
4. The ultimate load of specimens with the 25 mm diameter dowel bar and the stainless steel ring cannot be fully utilised in practice due to the large ultimate displacement Δ_u and the ultimate to yield displacement ratio Δ_u/Δ_y.
5. A close relationship is found between the maximum concrete compressive stress and stainless steel ring thickness under 20 kN service load.

According to the observations from the parametric analysis, equations to predict the ultimate load and the maximum compressive stress under service load are proposed. The design of removable dowel bar connection system could follow these equations to evaluate the ultimate load of specimen under ultimate limit state (ULS) and assess the concrete compressive behaviour under 20 kN service limit state (SLS). Through this two-stage design, the design of removable dowel bar connection systems will be more durable.

Acknowledgement

The research work presented in this paper was supported by a grant from the Research Grants Council of the Hong Kong Special Administrative Region, China (Project no. R5007-18). The authors would like to sincerely acknowledge the advice on the joint design from Professor Yuhong Wang at The Hong Kong Polytechnic University. The authors would also like to thank the technical staff, Mr. H.Y. Leung, Mr. K.H. Wong of the Structural Engineering Research Laboratory and Concrete Technology laboratory for their support as well as

350 the support from the Industrial Center at The Hong Kong Polytechnic University.

351

References

[1] AASHTO. AASHTO guide for design of pavement structure. Washington D.C: American Association of State Highway and Transportation Officials; 1993.

[2] Tayabji S, Ye D, Buch N. Precast Concrete Pavement Technology. Washington, DC: Transportation Research Board; 2013.

[3] Smith P, Snyder MB. Manual for Jointed Precast Concrete Pavement. National Precast Concrete Association; 2019.

[4] Syed A, Sonparote R. A Review of Precast Concrete Pavement Technology. Baltic Journal of Road Bridge Engineering 2020;15:22-53.

[5] Ioannides A. M., Korovesis G. T. Analysis and design of doweled slab-on-grade pavement systems. Journal of Transportation Engineering 1992; 118, 745-768.

[6] ACI Committe 325. Guide for Design of Jointed Concrete Pavements for Streets and Local Roads. American Concrete Institute; 2002.

[7] Snyder M. B. Guide to dowel load transfer systems for jointed concrete roadway pavements. 2011.

[8] Yin W., Lu H., Yuan J., Huang B. Mechanical characteristics of dowel bar-concrete interaction: based on substructure experiment. International Journal of Pavement Engineering 2020; 1-13.

[9] Shoukry S. N., William G., Riad M. Characteristics of concrete contact stresses in doweled transverse joints. International Journal of Pavement Engineering 2002; 3, 117-129.

[10] Al-Humeidawi B. H., Mandal P. Evaluation of performance and design of GFRP dowels in jointed plain concrete pavement–part 2: numerical simulation and design considerations. International Journal of Pavement Engineering 2014; 15, 752-765.

373 [11] Porter M., Pierson N. Laboratory evaluation of alternative dowel bars for use in Portland cement
374 concrete pavement construction. Transportation research record 2007; 2040, 80-87.
375 [12] Khazanovich L., Yut I., Tompkins D., Schultz A. Accelerated loading testing of stainless steel hollow
376 tube dowels. Transportation research record 2006; 1947, 101-109.
377 [13] Harrington J. F. Comparison of alternative laboratory dowel bar testing procedures. 2006.
378 [14] Al-Humeidawi B. H., Mandal P. Evaluation of performance and design of GFRP dowels in jointed
379 plain concrete pavement–part 1: experimental investigation. International Journal of Pavement
380 Engineering 2014; 15, 449-459.
381 [15] Friberg B., Richart F., Bradbury R. Load and deflection characteristics of dowels in transverse joints
382 of concrete pavements. Highway Research Board Proceedings, 1939.
383 [16] Mackiewicz P. Finite-element analysis of stress concentration around dowel bars in jointed plain
384 concrete pavement. Journal of Transportation Engineering 2015; 141, 06015001.
385 [17] Priddy L. P., Doyle J. D., Flintsch G. W., Pittman D. W., Anderton G. L. Three-dimensional modelling
386 of precast concrete pavement repair joints. Magazine of Concrete Research 2015; 67, 513-522.
387 [18] Riad M. Y., Shoukry S. N., William G. W., Fahmy M. R. Effect of skewed joints on the performance
388 of jointed concrete pavement through 3D dynamic finite element analysis. International Journal of
389 Pavement Engineering 2009; 10, 251-263.
390 [19] Li LK, Tan YQ, Gong XB, Li YL. Characterization of Contact Stresses Between Dowels and
391 Surrounding Concrete in Jointed Concrete Pavement. 2012.
392 [20] Hu C., Ma J., Zhao J., Leng Z., Jelagin D. Experimental study of dowel bar alternatives based on
393 similarity model test. Advances in Materials Science Engineering 2017; 2017.

394 [21] Murison S. Evaluation of concrete-filled GFRP dowels for jointed concrete pavements. 2004.
395 [22] Murison S., Shalaby A., Mufti A. Concrete-Filled, Glass Fiber–Reinforced Polymer Dowels for Load
396 Transfer in Jointed Rigid Pavements. Transportation research record 2005; 1919, 54-64.
397 [23] Brown V., Bartholomew C. FRP dowel bars in reinforced concrete pavements. Special Publication
398 1993; 138, 813-830.
399 [24] Eddie D., Shalaby A., Rizkalla S. Glass fiber-reinforced polymer dowels for concrete pavements. ACI
400 Structural Journal 2001; 98, 201-206.
401 [25] Benmokrane B, Ahmed EA, Montaigu M, Thebeau D. Performance of Glass Fiber-Reinforced
402 Polymer-Doweled Jointed Plain Concrete Pavement under Static and Cyclic Loadings. ACI Structural
403 Journal 2014;111:331-341.
404 [26] Porter ML. Testing Structural Behaviour of Alternative Dowel Bars. 2006.
405 [27] Huang Y., Wang S. Finite-element analysis of concrete slabs and its implications for rigid pavement
406 design. Highway Research Record 1973.
407 [28] Huang Y. H. A computer package for structural analysis of concrete pavements. Third International
408 Conference on Concrete Pavement Design and Rehabilitation. Purdue University, School of Civil
409 Engineering. 1985.
410 [29] Mahboub K. C., Liu Y., Allen D. L. Evaluation of temperature responses in concrete pavement. Journal
411 of Transportation Engineering 2004; 130, 395-401.
412 [30] Guo H., Sherwood J. A., Snyder M. B. Component dowel-bar model for load-transfer systems in PCC
413 pavements. Journal of Transportation Engineering 1995; 121, 289-298.
414 [31] Tabatabaie A. M., Barenberg E. Finite-element analysis of jointed or cracked concrete pavements.

Transportation Research Record 1978.

[32] Tayabji S. D., Colley B. E. Analysis of jointed concrete pavements. 1986.

[33] Tia M., Armaghani J. M., Wu CL., Lei S., Toye K. L. FEACONS III computer program for analysis of jointed concrete pavements. Transportation Research Record 1987.

[34] Zaman M., Alvappillai A. Contact-element model for dynamic analysis of jointed concrete pavements. Journal of transportation engineering 1995; 121, 425-433.

[35] Nishizawa T., Fukuda T., Matsuno S. A refined model of doweled joints for concrete pavement using FEM analysis. proceedings, 4th International Conference on Concrete Pavement Design and Rehabilitation, Purdue University, April 18-20, 1989.

[36] Guo H., Larson R., Snyder M. A nonlinear mechanistic model for dowel looseness in PCC pavements. Fifth International Conference on Concrete Pavement Design and Rehabilitation, Purdue University, School of Civil Engineering. 1993.

[37] Bhattacharya K. Nonlinear response of transverse joints of airfield pavements. Journal of transportation engineering 2000; 126**,** 168-177.

[38] Channakeshava C., Barzegar F., Voyiadjis G. Z. Nonlinear FE analysis of plain concrete pavements with doweled joints. Journal of Transportation Engineering 1993; 119, 763-781.

[39] Kuo CM., Hall K. T., Darter M. I. Three-dimensional finite element model for analysis of concrete pavement support. Transportation Research Record 1995.

[40] Maitra S. R., Reddy K., Ramachandra L. Load transfer characteristics of dowel bar system in jointed concrete pavement. International Journal of Fracture 2009; 135, 813-821.

[41] Nishizawa T., Koyanagawa M., Takeuchi Y., Kimura M. Study on mechanical behaviour of dowel bar

436 in transverse joint of concrete pavement. Proceedings of the 7th International Conference on Concrete
437 Pavements, Orlando, FL, 2001.
438 [42] Davids W. G. 3D finite element study on load transfer at doweled joints in flat and curled rigid
439 pavements. International Journal of Geomechanics 2001; 1, 309-323.
440 [43] Davids W. G., Wang Z., Turkiyyah G., Mahoney J. P., Bush D. Three-dimensional finite element
441 analysis of jointed plain concrete pavement with EverFE2. 2. Transportation Research Record 2003;
442 1853, 92-99.
443 [44] Kim J., Hjelmstad K. D. Three-dimensional finite element analysis of doweled joints for airport
444 pavements. Transportation Research Record 2003; 1853, 100-109.
445 [45] Kim K., Chun S., Han S., Tia M. Effect of dowel bar arrangements on performance of jointed plain
446 concrete pavement (JPCP). International Journal of Concrete Structures 2018; 12, 1-11.
447 [46] Mackiewicz P., Szydło A. The analysis of stress concentration around dowel bars in concrete pavement.
448 Magazine of Concrete Research 2020; 72, 97-107.
449 [47] Mackiewicz P. Analysis of stresses in concrete pavement under a dowel according to its diameter and
450 load transfer efficiency. Canadian Journal of Civil Engineering 2015; 42, 845-853.
451 [48] Prabhu M., Varma A. & Buch N. Analytical investigation of the effects of dowel misalignment on
452 concrete pavement joint opening behaviour. International Journal of Pavement Engineering 2009; 10,
453 49-62.
454 [49] Prabhu M., Varma A. H., Buch N. Experimental and analytical investigations of mechanistic effects of
455 dowel misalignment in jointed concrete pavements. Transportation research record 2007; 2037, 12-29.
456 [50] Sadeghi V., Hesami S. Finite element investigation of the joints in precast concrete pavement.

457 Computers Concrete 2018; 21, 547-557.
458 [51] Sadeghi V., Hesami S. Investigation of load transfer efficiency in jointed plain concrete pavements
459 (JPCP) using FEM. International Journal of Pavement Research Technology 2018; 11, 245-252.
460 [52] Saxena P., Hoegh K., Khazanovich L., Gotlif A. Laboratory and finite element evaluation of joint
461 lockup. Transportation research record, 2095, 34-42.
462 [53] Shoukry S. N., William G. W., Riad M. Application of LS-DYNA in Identifying Critical Stresses
463 Around Dowel Bars. 8th Int. LS-DYNA Users Conference, 2011.
464 [54] Zhou ZF. Stress concentration analysis in concrete round dowels for airport jointed rigid pavement
465 system. ICTE 2011.
466 [55] El-Hamrawy S. A., El-Maaty A. E. A., Hekal G. M., Salah El-Din E. M. 3D Modelling and Analysis
467 of Jointed Rigid Airfield Pavement using ABAQUS. The International Conference on Civil and
468 Architecture Engineering, Military Technical College, 1-14, 2016.
469 [56] Guo J.C., Chan T.M.. Experimental and numerical study on the structural performance of the stainless
470 steel ring strengthened removable dowel bar connection system. International Journal of Pavement
471 Engineering. (Under review).
472 [57] ABAQUS 6.14, Dassault Systems, Waltham, MA, USA, 2014.
473 [58] Al-Humeidawi B. H., Mandal P. Numerical evaluation of the combined effect of dowel misalignment
474 and wheel load on dowel bars performance in JPCP. Engineering Structures 2022; 252, 113655.
475 [59] Lubliner J., Oliver J., Oller S., Onate E. A plastic-damage model for concrete. International Journal of
476 solids structures 1989; 25, 299-326.
477 [60] Lee J., Fenves G. L. Plastic-damage model for cyclic loading of concrete structures. Journal of

478 engineering mechanics 1998; 124**,** 892-900.

479 [61] Debnath P. P., Chan TM. A comprehensive numerical approach for modelling blind-bolted CFST
480 connections. Structures 2021; 33, 2208-2225.

481 [62] Sümer Y., Aktaş M. Defining parameters for concrete damage plasticity model. Challenge Journal of
482 Structural Mechanics 2015; 1, 149-155.

483 [63] CEB-FIP 2010. Fib Model Code for Concrete Structures 2010. Ernst & Sohn, Wiley. 2013.

484 [64] CEB-FIP 1990. Model Code for Concrete Structures 1990. Ernst & Sohn, Wiley. 1993.

485 [65] ABAQUS 6.14, CAE User's Guide. Dassault Systems 2014.

486 [66] Birtel V., Mark P. Parameterised finite element modelling of RC beam shear failure. ABAQUS users'
487 conference, 2006.

488 [67] Gardner L., Cruise R. B., Sok C. P., Krishnan K., Ministro Dos Santos J. Life-cycle costing of metallic
489 structures. Proceedings of the Institution of Civil Engineers-Engineering Sustainability. Thomas
490 Telford Ltd, 167-177. 2007.

491 [68] Real E., Arrayago I., Mirambell E., Westeel R. Comparative study of analytical expressions for the
492 modelling of stainless steel behaviour. Thin-Walled Structures 2014; 83, 2-11.

493 [69] Zhao O., Gardner L., Young B. Structural performance of stainless steel circular hollow sections under
494 combined axial load and bending–Part 1: Experiments and numerical modelling. Thin-Walled
495 Structures 2016; 101, 231-239.

496 [70] Hradil P., Talja A., Real E., Mirambell E., Rossi B. Generalized multistage mechanical model for
497 nonlinear metallic materials. Thin-walled structures 2013; 63, 63-69.

498 [71] Quach W., Teng J. G., Chung K. F. Three-stage full-range stress-strain model for stainless steels.

499 Journal of Structural Engineering 2008; 134, 1518-1527.

500 [72] Rasmussen K. J. Full-range stress–strain curves for stainless steel alloys. Journal of constructional steel
501 research 2003; 59, 47-61.

502 [73]. Azizinamini A, Darwin D, Eligehausen R, Pavel R, Ghosh SK. Proposed modifications to ACI 318-95
503 tension development and lap splice for high-strength concrete. 1999.

504 [74]. Park R. Evaluation of ductility of structures and structural assemblages from laboratory testing.
505 Bulletin of the new Zealand society for earthquake engineering 1989;22:155-166.

506 [75] Zuzulova A., Grosek J., Janku M. Experimental laboratory testing on behaviour of dowels in concrete
507 pavements. Materials 2020; 13, 2343.

508 [76] American Concrete Institute Committee 325. Structural Design Considerations for Pavement Joints.
509 Journal of the American Concrete Institute, Vol. 28, No. 1, July 1956, pp. 1–28.

510 [77] Smith K. D., Harrington D. S., Pierce L., Ram P., Smith K. L. Concrete Pavement Preservation Guide.
511 United States. Federal Highway Administration. 2014.

512 [78] Lee M., Barr B. An overview of the fatigue behaviour of plain and fibre reinforced concrete. Cement
513 Concrete Composites 2004; 26, 299-305.

514